Tellus (1986), *38A*, 412–428

Energetics analysis of the observed and simulated general circulation using three-dimensional normal mode expansions

By HIROSHI TANAKA, ERNEST C. KUNG, *Department of Atmospheric Science, University of Missouri-Columbia, Columbia, Missouri 65211, USA* and WAYMAN E. BAKER, *Laboratory for Atmospheres, NASA/Goddard Space Flight Center, Greenbelt, Maryland 20771, USA*

(Manuscript received September 16, 1985; in final form January 28, 1986)

ABSTRACT

The energetics characteristics of the observed and simulated general circulation are analyzed using three-dimensional normal mode expansions. The data sets involved are the Goddard Laboratory for Atmospheres (GLA) analysis and simulation data and the Geophysical Fluid Dynamics Laboratory (GFDL) analysis data. The spectral energy properties of the Rossby and gravity modes and energy transformations are presented.

Significant influences of model characteristics and the assimilation techniques are observed in the barotropic energy spectrum, particularly for the gravity mode. Energy transformations of the zonal mean field in the GLA analysis and simulation are similar, but distinctly different from that in the GFDL analysis. However, overall, the energy generation in the baroclinic mode is largely balanced by the sink in the barotropic mode. The present study may demonstrate utilities of the three-dimensional normal mode energetics in the analysis of the general circulation.

1. Introduction

Analysis of energy and its transformations in terms of three-dimensional normal mode functions (3-D NMF) offers a new approach to an energy diagnosis of the general circulation. Earlier Kasahara (1976) applied Hough functions to an orthonormal basis for decomposition of energy in the meridional mode domain. After Kasahara and Puri (1981) obtained orthonormal eigensolutions for the vertical structure equations, it has become possible to represent atmospheric data by expansion into three-dimensional harmonics of eigensolutions. Tanaka (1985) reported our energy diagnosis scheme using 3-D NMF, which not only analyzes the energy components of the Rossby and gravity modes but also examines energy transformations in and among the 3-D NMF. This normal mode energetics scheme was applied to the First GARP (Global Atmospherics Research Program) Global Experiment (FGGE) data produced by the Geophysical Fluid Dynamics Laboratory (GFDL).

The normal modes are the eigensolutions of linearized primitive equations over a sphere. The normal mode energetics scheme unifies three one-dimensional spectral energetics schemes in domains of the wavenumber, meridional mode and vertical mode. The associated eigenfrequency also enables us to examine the energetics in the frequency domain. Despite the known deficiencies, such as the use of basic state at rest to derive the 3-D NMF, Tanaka's (1985) paper indicates the potential usefulness of the normal mode energetics scheme. Energy conversions are measured between the baroclinic mode and barotropic mode, and between the zonal and eddy components of available potential energy and kinetic energy.

However, it is anticipated that the normal mode energetics may be influenced by the assimi-

lation of the observation data. The gravity mode particularly is very model dependent and responds sensitively to the nonlinear normal mode initialization process. The Goddard Laboratory for Atmospheres (GLA) provides FGGE IIIb analysis (assimilation) data without using the nonlinear normal mode initialization. Thus, the energetic comparison between the GFDL and GLA analyses will offer interesting information about the sensitivity of the general circulation model (GCM) employed. The energetics comparison between the simulated and the observed circulation with the same GCM also provides useful information on the energetics similarity and dissimilarity of the simulation to the observation. In this study, the normal mode energetics scheme is applied to the GLA IIIb analysis data of the FGGE observations and a parallel model simulation for the same 25-day period in January 1979. The results of the energetics analysis are compared for the analysis and simulation, and further with a diagnosis of the GFDL data. The energetics characteristics and the contrasts of these data sets are examined with an emphasis on the gravity mode energy and energy interactions within and between various modes. Finally, the utility of the normal mode energetics scheme supplement of the standard spectral energetics diagnosis is discussed.

2. Data sets for the observed and simulated atmospheres

The GLA IIIb analysis of the FGGE observations for a 25-day period, 5–29 January 1979, and the GLA simulation for the same period were utilized for the energetics analysis of this study. The simulation experiment with the GLA GCM was integrated from initial conditions for 00.00 GMT 15 December 1978, which were provided by the European Center for Medium Range Weather Forecast FGGE IIIb analyses (see Bengtsson et al., 1982). The selected 25-day period represents the 21st–45th days of the simulation after the initialization of the model. During this period, the simulation is well beyond the period of initial adjustment. In order to obtain a basic state temperature profile for computation of vertical eigenfunctions and Hough vector functions, the global mean temperature of the GLA analysis is obtained for the four months of 5 January–5 March and 1 June–31 July 1979, and its vertical distribution is listed in Table 2.

The objective analysis scheme to assimilate the GLA IIIb analysis data is described in detail by Baker (1983). In summary, eastward and northward wind components, geopotential height, and relative humidity are analyzed on mandatory pressure surfaces with the first guess field provided by the model 6-hour forecast. Surface pressure and temperature are reduced to sea surface level for analysis. The analysis at each level is performed with the Cressman (1959) successful correction method, which is modified to account for differences in the data density and the statistical estimates of the error structure of observations. The GCM utilized in the data assimilation and model experiment is the fourth-order global atmospheric model as described by Kalnay-Rivas et al. (1977) and Kalnay-Rivas and Hoitsma (1979), and more recently by Kalnay et al. (1983). There are 9 vertical layers equal in sigma with a uniform non-staggered horizontal grid (4° latitude by 5° longitude). The model is based on an energy-conserving scheme in which all horizontal differences are computed with 4th-order accuracy. A 16th-order Shapiro (1970) filter is applied every 2 h on the sea level pressure, potential temperature and wind fields. In this scheme, wavelengths longer than 4 grid lengths are resolved accurately without damping. Wavelengths shorter than 4 grid lengths, which would otherwise be grossly misrepresented by the finite differences, are filtered out while they are still infinitesimal.

The GLA analysis and simulation data used in this study include daily grid-point values of geopotential height, temperature, humidity, wind and vertical velocity at 1000, 850, 700, 500, 400, 300, 250, 200, 150, 100, 70 and 50 hPa at 00.00 GMT. In this paper, references are made to the GFDL IIIb analysis of the observed atmosphere (Ploshay et al., 1983). The normal mode energetics of 3 winter months computed by Tanaka (1985) from the GFDL data are utilized for this purpose.

3. Scheme of analysis

The scheme of analysis has been detailed in Tanaka (1985), and only an abbreviated description is provided in this section. Symbols, defini-

tions and variables used in this paper are listed in Table 1. By obtaining 3-D NMF on a basic state at rest (see Kasahara and Puri, 1981), sets of vertical and Fourier-Hough transforms are constructed, based on the orthonormality of the eigenfunctions, i.e.,

$$f(p) = \sum_{m=0}^{\infty} f_m G_m(p), \tag{1}$$

$$f_m = \frac{1}{p_s} \int_0^{p_s} f(p) G_m(p) \, dp, \tag{2}$$

and

$$\boldsymbol{W}_m(\lambda, \theta, t) = \sum_{r=0}^{\infty} \sum_{s=-\infty}^{\infty} w_{srm}(t) \boldsymbol{H}_{srm}(\lambda, \theta), \tag{3}$$

$$w_{srm}(t) = \frac{1}{2\pi} \int_{-\pi/2}^{\pi/2} \int_0^{2\pi} \boldsymbol{W}_m(\lambda, \theta, t) \cdot \boldsymbol{H}^*_{srm}(\lambda, \theta) \times \cos\theta \, d\lambda \, d\theta, \tag{4}$$

where $G_m(p)$, $\boldsymbol{H}_{srm}(\lambda, \theta)$ are vertical eigenfunctions and Hough harmonics, and f_m, w_{srm} are the corresponding expansion coefficients for arbitrary functions of $f(p)$ and $\boldsymbol{W}_m(\lambda, \theta, t)$. The subscripts s, r and m denote the zonal wavenumber, meridional mode index and vertical mode index, respectively, and the asterisk denotes the complex conjugate.

The basic state temperature T_0, stability parameter γ and equivalent height h_m are listed in Table 2. Indication of the tropopause is not apparent for the global mean state in Table 2. This is due to the lack of sufficient model resolution in the stratophere. Fig. 1 illustrates the orthonormal vertical eigenvectors obtained by the finite difference scheme with 12 vertical levels. The vertical mode $m = 0$ is regarded as the barotropic

Table 1. *Symbols, definitions and variables*

λ	longitude
θ	latitude
p	pressure
t	time
u	zonal wind speed
v	meridional wind speed
$\boldsymbol{V}$	horizontal wind vector
ω	vertical p-velocity
T	perturbation temperature
ϕ	perturbation geopotential
z	perturbation geopotential height
g	gravity of the earth
R	specific gas constant
c_p	specific heat at constant pressure
Ω	angular speed of the earth's rotation
T_0	temperature of basic state
γ	stability parameter $\gamma = RT_0/c_p - p\mathrm{d}T_0/\mathrm{d}p$
p_s	surface pressure of basic state
S	whole area of isobaric surface
s	zonal wavenumber
r	meridional mode index
m	vertical mode index
h_m	equivalent height
G_m	vertical eigenvector
f	arbitrary function of p
f_m	vertical transform of f
i	imaginary unit
$(\quad)^T$	transpose of a vector
$(\quad)^*$	complex conjugate
E	total energy $A + K$
A	available potential energy
K	kinetic energy $K_u + K_v$
K_u	kinetic energy of u-component
K_v	kinetic energy of v-component
β	energy ratio of Hough function $\beta_u + \beta_v + \beta_z = 1$
σ_{srm}	dimensionless eigenfrequency scaled by 2Ω
$(U, -iV, Z)^T$	Hough vector function
$\boldsymbol{H}_{srm}$	Hough harmonics $(U, -iV, Z)^T \exp(is\lambda)$
$\boldsymbol{W}_m$	vertical transform of variable vector $(u, v, \phi)^T$
w_{srm}	Fourier-Hough transform of $\boldsymbol{W}_m$
b_{srm}	vertical and Fourier-Hough transform of nonlinear term vector of wind field
c_{srm}	vertical and Fourier-Hough transform of nonlinear term vector of mass field
d_{srm}	vertical and Fourier-Hough transform of friction and diabatic heating vector
B_{srm}	nonlinear mode-mode interaction of kinetic energy
C_{srm}	nonlinear mode-mode interaction of available potential energy
D_{srm}	energy source and sink

Table 2. *Basic state temperature T_0, stability parameter γ and equivalent height h_m*

p(hPa)	T_0(K)	γ(K)	m	h_m(m)
50	208.22	53.18	0	9564.8
70	210.42	53.44	1	1629.1
100	212.75	53.98	2	338.6
150	215.52	49.54	3	163.6
200	220.50	39.53	4	92.5
250	227.10	31.19	5	64.6
300	233.95	25.94	6	47.8
400	247.54	22.14	7	28.1
500	258.44	24.76	8	21.9
700	274.23	32.45	9	14.4
850	282.80	35.13	10	10.6
1000	290.40	32.28	11	8.6

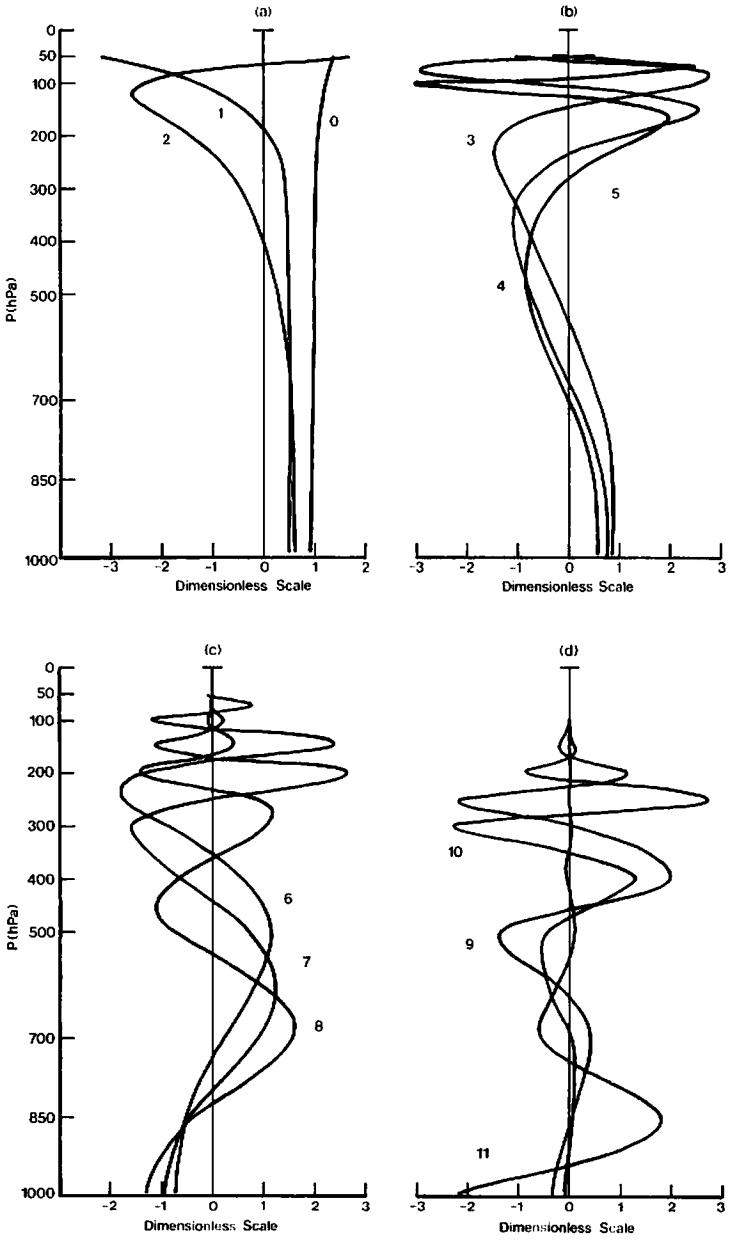

Fig. 1. Vertical eigenvectors for (a) vertical modes $m = 0$–2, (b) $m = 3$–5, (c) $m = 6$–8 and (d) $m = 9$–11.

mode, and $m \geqslant 1$ as the baroclinic modes. The structure is deformed by relatively low top level of 50 hPa (see Kasahara, 1984; Tanaka, 1985).

Applying proper dimensional factors of the equivalent height h_m and angular speed of the earth's rotation Ω to these transforms, the dimensionless primitive equation by the spectral representation becomes

$$\frac{d}{dt} w_{srm} + i\sigma_{srm} w_{srm} = b_{srm} + c_{srm} + d_{srm}, \tag{5}$$

where the complex variables w_{srm}, b_{srm}, c_{srm} and d_{srm} are the vertical and Fourier-Hough transforms of dependent variables u, v and ϕ, non-linear terms

due to wind fields, nonlinear terms due to mass fields, and diabatic processes, respectively (see Table 1). The symbols i and σ_{srm} represent imaginary unit and dimensionless eigenfrequency obtained as a solution of Laplace's tidal equation with a basic state at rest.

The corresponding energy balance equation with dimensional form is given by

$$\frac{d}{dt} E_{srm} = B_{srm} + C_{srm} + D_{srm}, \tag{6}$$

where

$$E_{srm} = \tfrac{1}{2} p_s h_m |w_{srm}|^2, \tag{7}$$

$$B_{srm} = p_s \Omega h_m [w^*_{srm} b_{srm} + w_{srm} w^*_{srm}], \tag{8}$$

$$C_{srm} = p_s \Omega h_m [w^*_{srm} c_{srm} + w_{srm} c^*_{srm}], \tag{9}$$

$$D_{srm} = p_s \Omega h_m [w^*_{srm} d_{srm} + w_{srm} d^*_{srm}], \tag{10}$$

The energy of a normal mode E_{srm} as defined in (7) includes multiplication by a dimensional factor of h_m and global mean surface pressure p_s so that the energy may be expressed in physical units. According to (6), the time change of E_{srm} is caused by the nonlinear mode-mode interaction of the kinetic energy B_{srm}, available potential energy C_{srm} and energy source and sink due to the diabatic process D_{srm}, including dissipation. Since σ_{srm} in (5) is always real (Matsuno, 1966a), the linear term on the left-hand side of (5) does not contribute to the time change of energy. The right-hand sides of eqs. (7)–(10) should be multiplied by 0.5 for $s = 0$.

The kinetic energy of zonal and meridional components K_u and K_v, and the available potential energy A for each mode can be retrieved by E_{srm} through multiplication with β_u, β_v, and β_z, which represent the vector norms of the normalized Hough vector functions $U(\theta)$, $V(\theta)$ and $Z(\theta)$:

$$\begin{bmatrix} K_u \\ K_v \\ A \end{bmatrix}_{srm} = E_{srm} \begin{bmatrix} \beta_u \\ \beta_v \\ \beta_z \end{bmatrix}_{srm} = E_{srm} \int_{-\pi/2}^{\pi/2} \begin{bmatrix} U^2 \\ V^2 \\ Z^2 \end{bmatrix}_{srm} (\theta) \times \cos\theta \, d\theta, \tag{11}$$

where $\beta_u + \beta_v + \beta_z = 1$.

By means of the inverse transforms of the vertical and Fourier-Hough transforms, it can be proven that

$$\sum_{m=0}^{\infty} \sum_{r=0}^{\infty} \sum_{s=0}^{\infty} B_{srm} = \frac{1}{gS} \int_S \int_0^{p_s} \left[-\nabla \cdot K\boldsymbol{V} - \frac{\partial}{\partial p} K\omega \right] \times dp \, dS = 0, \tag{12}$$

$$\sum_{m=0}^{\infty} \sum_{r=0}^{\infty} \sum_{s=0}^{\infty} C_{srm} = \frac{1}{gS} \int_S \int_0^{p_s} \left[-\nabla \cdot A\boldsymbol{V} - \frac{\partial}{\partial p} A\omega \right] \times dp \, dS = 0, \tag{13}$$

The vertical change of γ and vertical geopotential flux across the surface boundary have been neglected in order to get the relation (13). The diabatic term D_{srm} is evaluated as the residual balance of (6) in this study. The positive B_{srm}, C_{srm} and D_{srm} represent an increase of E_{srm} or energy supply into the mode by these terms.

4. Energy distributions

A summation of energies for all normal modes is equivalent to the energy integrated over the entire mass of the atmosphere. If we take a summation of energies for all meridional and vertical modes with respect to each zonal wavenumber, the resultant energy becomes a function only of the wavenumber. It provides spectral distributions of energy similar to the standard analysis in the zonal wavenumber domain (Saltzman, 1957), except that the present method provides the energy distributions of gravity and Rossby modes separately.

The spectral distributions of kinetic energy for the Rossby and gravity modes are illustrated in Fig. 2 as a function of wavenumber for GLA analysis and simulation. The kinetic energy of gravity modes by the GFDL analysis is also presented in the figure for comparison. The Rossby mode by the GFDL analysis is omitted because the spectrum is nearly identical to the GLA analysis. The kinetic energy spectra of the Rossby mode approximately follow the -3 power of the wavenumber. This range is regarded as an inertial subrange for two-dimensional isotropic turbulence in the atmosphere (e.g., Leith, 1971; Wiin-Nielsen, 1967). The spectra of the gravity mode follow the $-5/3$ power law.

From spectral distributions of kinetic energy in Fig. 2, the following two points seem to stand out. First, the energy level of the gravity mode of the GLA analysis is consistently higher than that of the simulation. The energy level of the GFDL analysis is closer to that of the GLA simulation. The $-5/3$ power law of the gravity modes approximately holds for both the GFDL and GLA analyses, even though the former utilizes the nonlinear normal mode initialization to adjust the gravity modes, and the latter does not. Second, the kinetic energy level at wavenumber 1 for the Rossby mode of simulation is about half that for observation. This corroborates the finding of the inability of the model to simulate the rapid amplification of wavenumber 1 as it appears in the observed winter atmosphere (Labitzke, 1982).

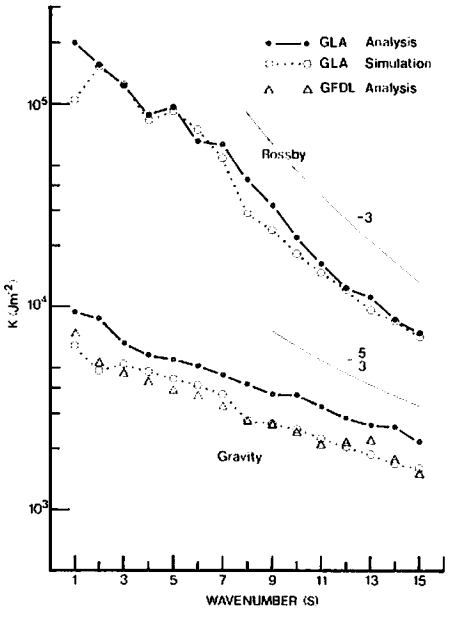

Fig. 2. Kinetic energy distributions in the wavenumber domain for the GLA analysis and simulation. Kinetic energy of gravity modes by GFDL analysis is after Tanaka (1985).

Fig. 3 illustrates the time changes of total energy E of wavenumber 1 for the barotropic mode ($m = 0$) and the first baroclinic (internal) mode ($m = 1$). The latter may be called a stratospheric mode, since it indicates large amplitudes in the stratosphere (see Fig. 1a). For the GLA analysis, the energy of the barotropic mode shows two peaks on 11 and 16 January and decreases after the latter peak, while the energy of the stratospheric mode increases rapidly during the end of January. The observed amplification and vertical propagation of wavenumber 1 during the end of January 1979 (Labitzke, 1982) are thus associated with the energy increase of the stratospheric mode $m = 1$. The first energy peak of $m = 0$ on

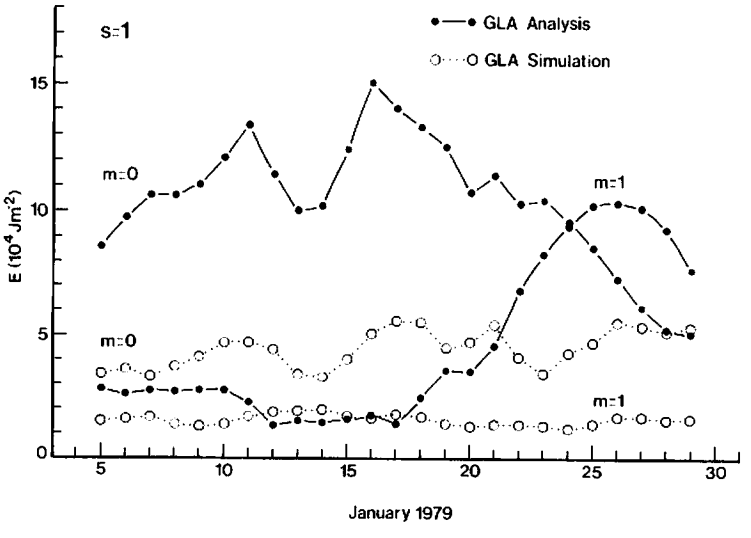

Fig. 3. Time change of total energy E of the barotropic mode ($m = 0$) and the stratospheric mode ($m = 1$) for wavenumber $s = 1$ of the GLA analysis and simulation.

11 January is caused by the amplification of meridional mode $r = 6$ of the Rossby mode, whereas the second peak on 16 January is due to $r = 4$ of the Rossby mode. This implies that the elongation of the meridional scale of the barotropic mode from $r = 6$ to 4 results in subsequent amplification of the stratospheric mode for the vertical propagation. However, the energy levels of the GLA simulation are maintained at their minimum levels for both $m = 0$ and $m = 1$ during this period. It is clear from Fig. 3 that a large part of the energy deficit at wavenumber 1 in the simulation is due to the low level of the barotropic mode $m = 0$, although the pattern of the time variation roughly agrees with that of the observation. The energy deficit at $m = 0$ can be related to the absence of the amplification of the stratospheric mode $m = 1$ in the simulation. It is possible that the coarse resolution in the stratosphere is responsible for the inability of the model to simulate wavenumber 1.

During the FGGE winter, the large-scale blockings were at full strength around 25 December, 9 January and 23 January (Hansen and Chen, 1982). Fig. 4 illustrates a typical blocking which appears in the observed circulation of the 9 January northern hemisphere. It is readily recognized that the amplified dipole structure of wavenumber 1 is superposed on wavenumber 2, creating a blocking high in the northern Pacific sector with an associated low south of it. On the other hand, most pronounced blocking in the simulation of 13 January in Fig. 4 shows a much weaker feature. The Ω-type blocking produced at 90°E is small and the structure is too marginal to be distinguished as a blocking high. In the simulated atmosphere, the model fails to simulate these large-scale blockings at the expected time, and when marginal blockings appear, they are deformed. The inability to simulate wavenumber 1, particularly for the barotropic mode, is associated with the failure to produce blocking.

The distributions of barotropic kinetic energy ($m = 0$) in the meridional mode domain are illustrated in Fig. 5 for wavenumbers $s = 1$–6. The distributions of the Rossby mode approximately follow the -3 power of the meridional mode index except for the very low index range. There are apparent energy peaks around $r = 3$–6. The Rossby mode energy spectra of the GLA

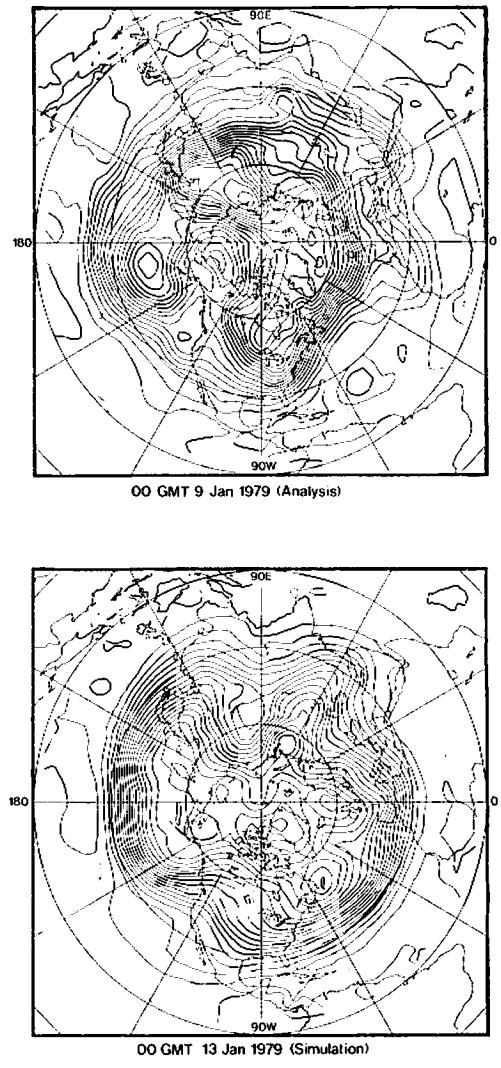

Fig. 4. Northern hemisphere 500 mb chart of the 9 January 1979 observation and 13 January 1979 simulation.

simulation are in good agreement with those of the GLA analysis, except at wavenumber 1 for which a lower energy peak of the simulation is indicated. A mixed Rossby gravity mode (see $r = 0$ of the Rossby mode) and antisymmetric global scale gravity modes (see odd numbers of r for the gravity mode) also show very low energy levels for wavenumber 1 of the simulation. The energy spectra for the gravity mode approximately follow the $-5/3$ power law, but the energy level of the gravity mode by the GLA analysis is one order

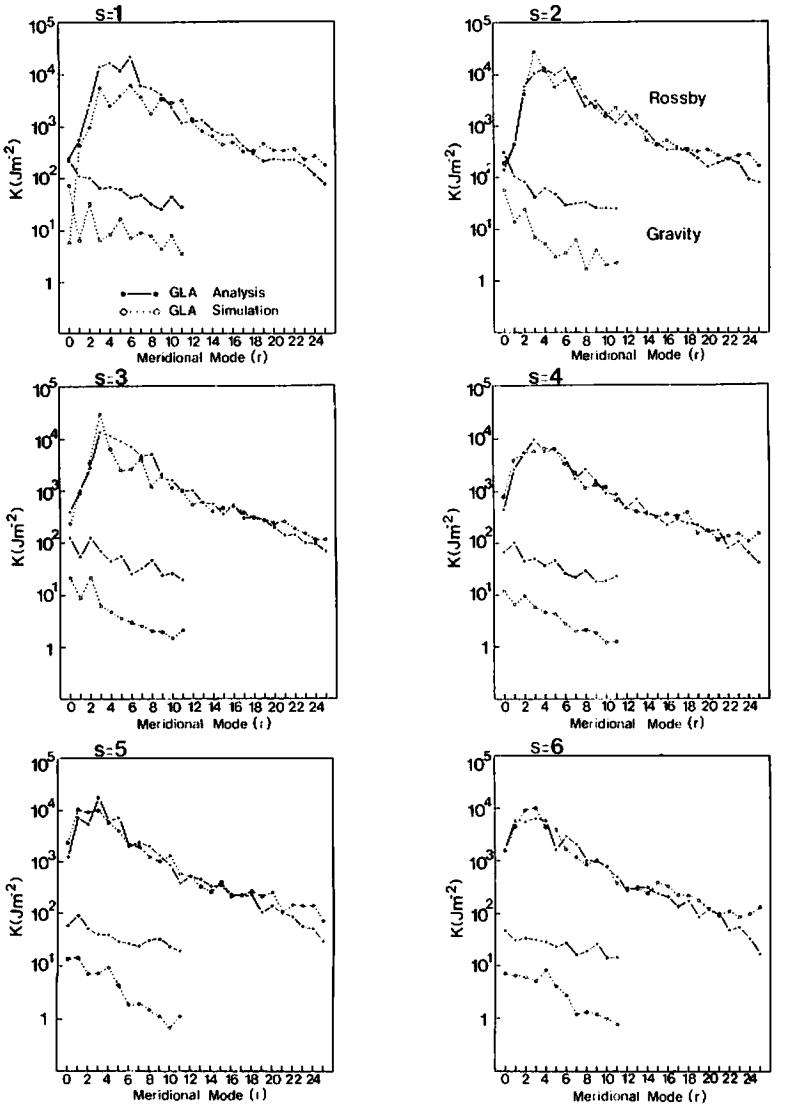

Fig. 5. Distributions of barotropic kinetic energy in the meridional mode domain for GLA analysis and simulation for wavenumbers $s = 1$–6.

higher than that of the simulation. As shown in Table 3, the barotropic kinetic energy level ($m = 0$) of the GFDL analysis is between those of the GLA analysis and simulation, while the GLA analysis shows more than three times larger barotropic energy than the GFDL analysis. It is also noted that the baroclinic kinetic energy ($m = 1$–11) of the GLA simulation and analysis is higher than that of the GFDL analysis. As shown in Table 3, the difference of the gravity mode kinetic energy among the GLA analysis, GLA simulation and GFDL analysis is significant at the 95% confidence level by means of a simple t-test for the time average. In the GFDL data, the energy level and distribution of gravity modes are prescribed by the global optimum interpolation in the final stage of the 4-dimensional assimilation process together with the nonlinear normal mode initialization (Miyakoda et al., 1982). However, they are prescribed by the Euler-backward time

Table 3. *Kinetic energy of barotropic ($m = 0$) and baroclinic ($m = 1$–11) gravity modes of the GLA simulation, GLA analysis and GFDL analysis by zonal wavenumber (s)*

	s	GLA simulation $m = 0$	GLA simulation $m = 1$–11	GLA analysis $m = 0$	GLA analysis $m = 1$–11	GFDL analysis $m = 0$	GFDL analysis $m = 1$–11
	1	1.8	64.2	8.5	85.9	3.8	70.8
	2	1.3	47.7	8.2	80.6	2.6	49.8
	3	0.8	51.1	6.3	61.0	1.8	45.1
	4	0.5	47.5	4.9	52.8	1.2	41.5
	5	0.6	43.6	4.6	50.6	1.0	38.0
	6	0.5	40.6	3.2	47.1	0.8	35.8
total	1–15	6.7	504.0	58.4	651.7	18.6	480.7
SD	1–15	0.7	33.9	7.0	46.7	5.2	46.8
CI (95%)	1–15	±0.3	±13.9	±2.9	±19.1	±0.8	±7.0

SD is the standard deviation of the time change of the total kinetic energy for $s = 1$–15 during the analysis periods. CI is the 95% confidence interval of deviation from the time average. Units: 10^2 J m^{-2}.

integration in the GLA analysis and simulation (Matsuno, 1966b). The 6-hour analysis/forecast assimilation cycle may be two short to damp the gravity modes in the GLA analysis in the high-frequency barotropic mode (see Table 3 and Fig. 6a). The absence of data insertion in the GLA simulation may result in the large damping of high-frequency gravity modes (Fig. 6b).

A Hough function is associated with an eigenfrequency which is determined by the

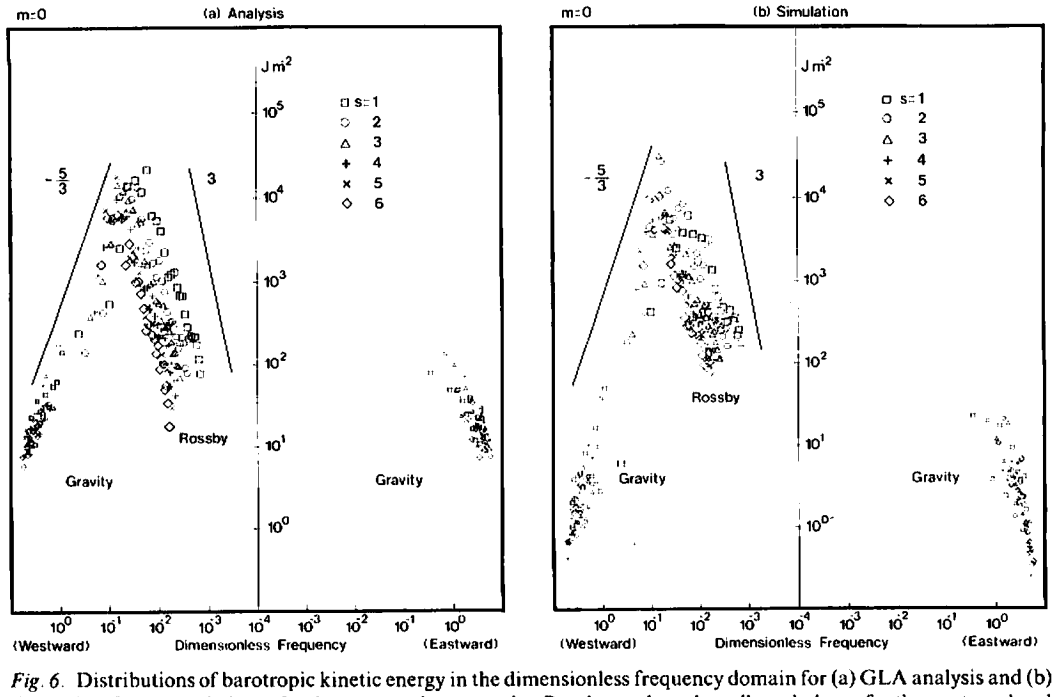

Fig. 6. Distributions of barotropic kinetic energy in the dimensionless frequency domain for (a) GLA analysis and (b) simulation. Large symbols are for the westward propagating Rossby mode and small symbols are for the westward and eastward propagating gravity modes for wavenumbers $s = 1$–6.

horizontal scale of waves. Using the eigenfrequency as a coordinate, we may investigate the energy spectra in the frequency domain. In Fig. 6, the kinetic energy distributions of barotropic modes for both the GLA analysis and simulation are plotted as a function of a dimensionless frequency. The westward propagating Rossby mode (large symbols) and gravity mode (small symbols) are plotted in the left half of each figure, whereas the eastward propagating gravity mode is plotted in the right half. Both Figs. 6a and 6b indicate clear energy peaks corresponding to those in the meridional mode domain (Fig. 5). The energy spectrum approximately follows the 3rd power of the frequency at the low-frequency range of the Rossby mode, whereas it follows the $-5/3$ power at the high-frequency range of the gravity mode. As found in Tanaka (1985) for the GFDL analysis, the high-frequency Rossby mode spectra follow the $-5/3$ power and merge with the spectra of the gravity mode without spectrum interruption. Despite these common features, it is noted that the energy level of the Rossby mode at very low frequency in the simulation is considerably higher than in the analysis, whereas that of the gravity mode at a very high frequency is much lower. As a result, the slope in the simulation is less than 3 at the low-frequency Rossby mode, but is steeper than $-5/3$ at the high-frequency gravity mode. The energy peak of the simulation also tends to shift towards a higher frequency than in the analysis. This seems to be related to the strong zonal wind of the GLA simulation if the energy peak in the frequency domain corresponds to the stationary waves.

5. Energy interactions

If we take a summation of energy interactions over all meridional and vertical modes, the resultant energy transformation becomes a function only of the zonal wavenumber. Such an interaction of the Rossby mode kinetic energy is presented separately for the barotropic ($m = 0$) and baroclinic ($m = 1$–11) modes in Fig. 7. The positive and negative values in the figure are for the gain and loss of energy at the specified wavenumber. The summation of $m = 0$ and $m = 1$–11 is equivalent to the sum of zonal-wave and wave-wave interactions of kinetic energy in the standard spectral energy scheme (i.e., Saltzman, 1957; Kung and Tanaka, 1983) except that the present results are for the Rossby mode only. The contribution from the gravity mode is found to be one to two orders smaller than that from the Rossby mode. The totals of energy interaction over $m = 0$–11 yield negative results for both the GLA analysis and simulation. This means the eddy kinetic energy is transformed into the zonal kinetic energy, or the latter gains at the expense of the former. The separation of the interactions into the barotropic and baroclinic modes reveals that this

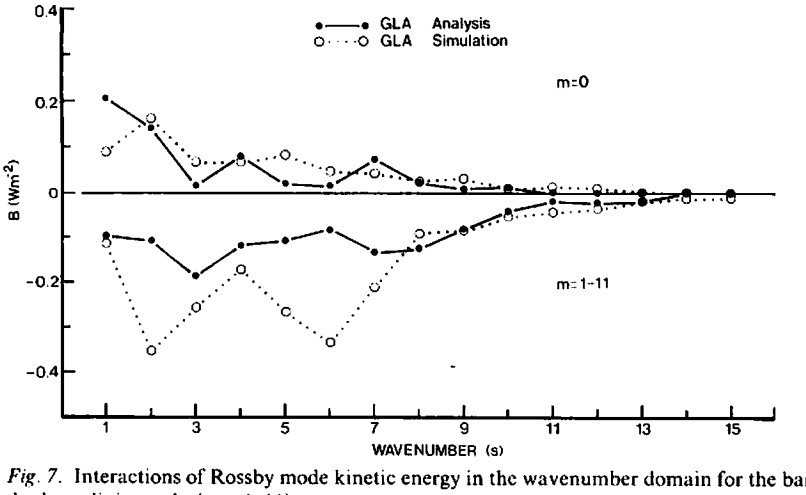

Fig. 7. Interactions of Rossby mode kinetic energy in the wavenumber domain for the barotropic mode ($m = 0$) and the baroclinic mode ($m = 1$–11).

overall feature is the same as for the baroclinic mode, but the direction of the barotropic energy is opposite to that of the baroclinic modes. Large differences between the GLA analysis and simulation are at wavenumbers 2 and 6 of the baroclinic mode. The intensity of the simulated energy transfer at these wavenumbers is about three times larger than that of the analysis. It is also noted that the energy supply into the barotropic mode at wavenumber 1 in the simulation is only about half that in the analysis. As a whole for $m = 0$–11, wavenumber 1 gains kinetic energy in the analysis data set, but shows an energy loss in the simulation. This deficit of the energy supply at wavenumber 1 is related to the low energy level of this wavenumber as seen in Fig. 2.

The interaction of kinetic energy is schematically illustrated in Fig. 8 as a function of wavenumber and vertical mode. Since the summation of all contributions is zero according to (12), the kinetic energy supply (negative values) may be associated with the gain (positive values) in the figure. The kinetic energy transformation from the baroclinic mode to the barotropic mode was studied by Smagorinsky (1963), Wiin-Nielsen (1962) and Kung (1966). They show that the kinetic energy of the baroclinic mode (in the shear flow), which is converted from the available potential energy, is transformed into the barotropic mode (the vertical mean flow). The arrows in Fig. 8 indicate the resultant kinetic energy transfer from the eddy baroclinic mode to the zonal barotropic mode. For the GLA analysis, a large amount of the eddy kinetic energy in the vertical modes $m = 2$ and 3 is converted into the zonal kinetic energy of the barotropic mode $m = 0$, while some limited amount is converted into the eddy kinetic energy of the barotropic mode. This is consistent with the feature demonstrated by Hoskins (1983) which shows that the zonal wind with vertical shear tends to be modifed towards the barotropic structure by the nonlinear baroclinic waves. The features in the GLA simulation are similar. However, a much stronger energy supply is shown distinctly at $m = 2$ for wavenumbers 2 and 6. As seen in Fig. 1, the vertical mode $m = 2$ has its peak below 100 hPa. For the GFDL analysis, $m = 2$ is a stratospheric mode (Tanaka, 1985) and the largest kinetic energy supply is at $m = 4$. The different structures of the vertical eigenfunctions between the GFDL and the GLA are caused by the different top levels of 30 mb and 50 mb, respectively, together with the different temperature profiles. The stratosphere is represented only by $m = 1$ in the GLA analysis and simulation.

Synthesizing energy interactions of the Rossby mode over all wavenumbers and meridional modes, we have the energy interaction among the vertical modes. In Fig. 9, the total diabatic process, including the energy generation (positive) by diabatic heating and dissipation (negative) due to the irreversible frictional process, is presented as a function of the vertical mode. This diabatic term is evaluated as the residual of the energy balance equation (6), taking account of the time change of the total energy. The total diabatic process for $s = 0$–15 in the figure is also separated into zonal ($s = 0$) and eddy ($s = 1$–15) contributions. Although the vertical structure functions are different for the GLA and GFDL data sets, the comparison among data sets may be qualitatively informative. The vertical modes higher than $m = 9$ have a problem of aliasing for the present discrete scheme as in Fig. 1d and are not utilized. However, this should not materially affect the results presented in this paper. It is readily seen that overall atmospheric energy is generated in the baroclinic modes ($m = 2$–4) and dissipated at the barotropic mode ($m = 0$). This is consistent with the view that the available potential energy is generated through the differential heating of the atmosphere and the kinetic energy is dissipated through friction, since the former is included in the baroclinic modes but the latter may be dominant in the barotropic mode. This energy flow from the baroclinic to barotropic modes is smaller in the GLA analysis and simulation than that in the GFDL analysis.

The separation of the total diabatic process into zonal mean ($s = 0$) and eddy ($s = 1$–15) components reveals significant differences among the GLA analysis and simulation and the GFDL analysis, especially in the zonal mean field. The GFDL analysis shows a notably larger energy generation in the baroclinic modes and a larger energy dissipation in the barotropic mode in the zonal component. For the GLA analysis and simulation, the energy generation in the baroclinic mode is smaller, but the barotropic mode also exhibits energy generation as a whole. The

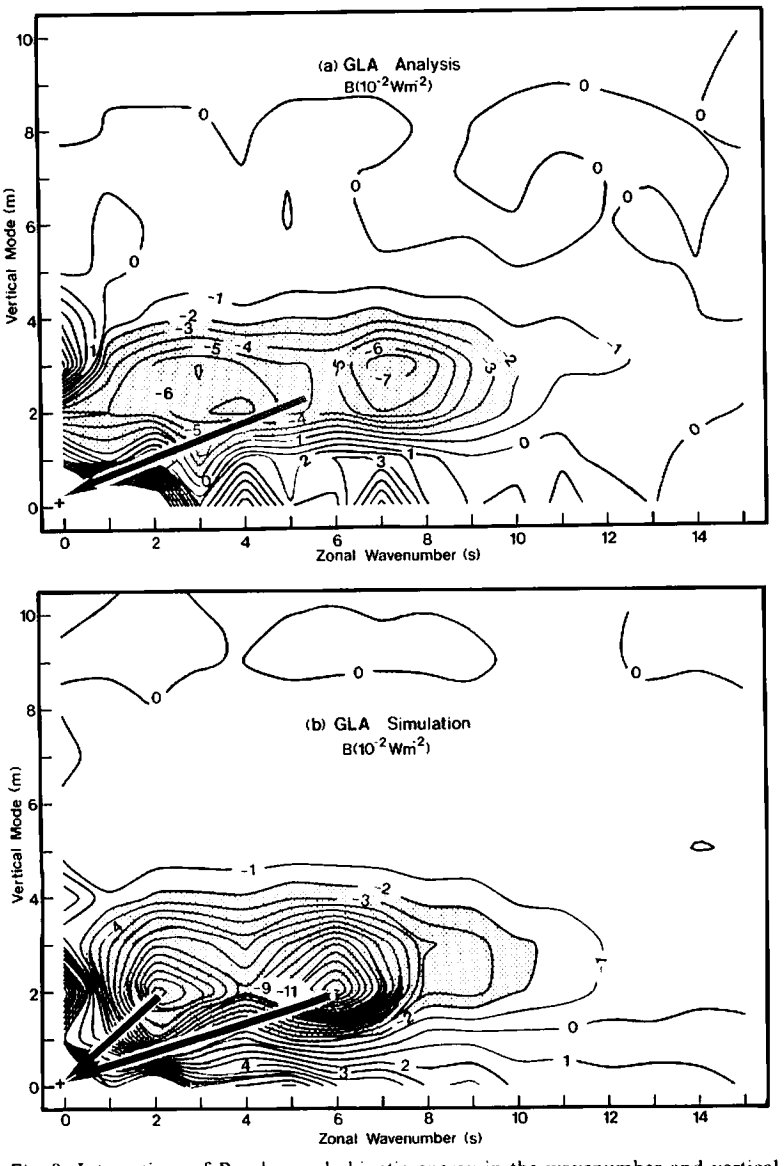

Fig. 8. Interactions of Rossby mode kinetic energy in the wavenumber and vertical mode domains for GLA (a) analysis and (b) simulation in units of 10^{-2} W m^{-2}.

statistical t-test for the time average of D for $s = 0$, $m = 0$ shows that the 95% confidence intervals are ± 0.19, ± 1.50 and ± 0.36 (W m^{-2}) for the GFDL analysis, GLA analysis and GLA simulation, respectively. Although the value for the GLA analysis fluctuates largely, the difference between the GFDL and the GLA is still significant. This may have resulted from the vertical profile of the diabatic heating of the zonal field being quite different between the GLA and GFDL analyses. For eddies, the GLA and GFDL analysis sets show better agreement, in that the energy is generated in the baroclinic modes and dissipated in the barotropic mode. Yet, the magnitude is generally smaller in the GFDL analysis. The overall energy flow as seen in Fig. 9 may be characterized as the energy generation in the baroclinic mode which seems to balance the

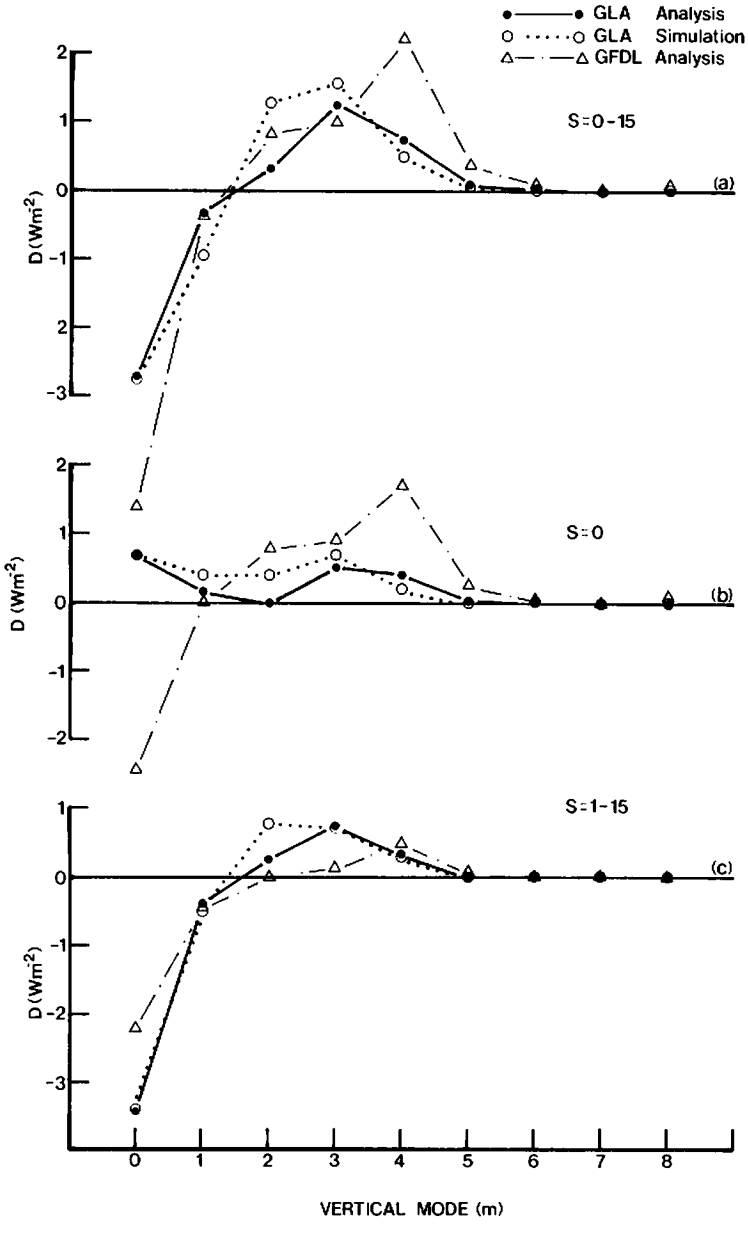

Fig. 9. Rossby mode diabatic process in the vertical mode domain for GLA analysis and simulation and GFDL analysis.

dissipation in the barotropic modes. However, a significant difference due to model characteristics seems to appear in the zonal mean field.

The eddy kinetic energy interactions in the meridional mode domain for the Rossby mode are presented in Fig. 10 for the GLA analysis and simulation. As in Fig. 7, the interactions are separated for the barotropic and baroclinic modes. We should note that, because the modal structures are altered, depending on the wavenumbers and the vertical modes, the meridional mode index does not simply represent the meridional scale of

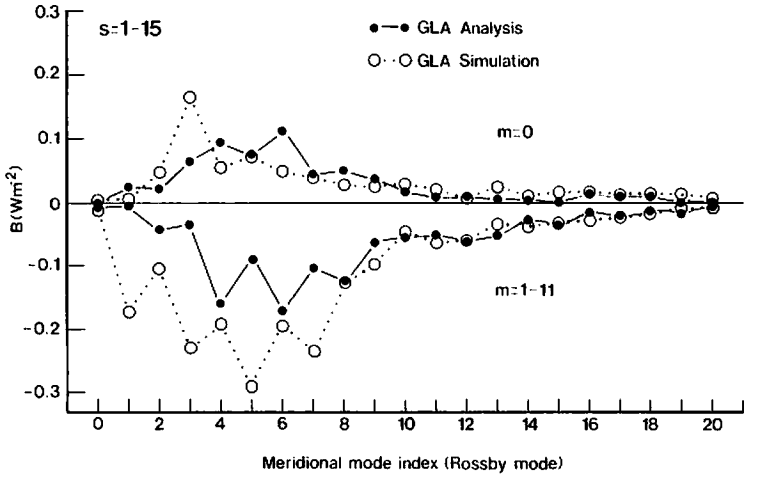

Fig. 10. Eddy kinetic energy interaction of the Rossby mode in the meridional mode domain for the barotropic mode ($m = 0$) and the baroclinic mode ($m = 1$–11).

the mode. Yet, the results show a characteristic distribution of small energy interactions at the low and high indices, but large interactions at the intermediate indices around $r = 3$–7 correspond to the energy peaks in Fig. 5. The interactions for the gravity modes are one order smaller than those for the Rossby mode. The results indicate a characteristic difference between the GLA analysis and simulation. The magnitude of the interactions due to the antisymmetric modes (even numbers) are large in the former, while those due to the symmetric modes (odd numbers) are large in the latter—where the modal symmetry is determined about the equator for zonal wind and geopotential fields. The large energy supply for zonal wind by the baroclinic modes of $s = 2$ and 6 in Fig. 7 of the GLA simulation is caused by the large interaction of these symmetric modes.

It may be pertinent to point out that the energy interaction in the meridional mode domain is less important than in the wavenumber and vertical mode domains. We observe clear energy interactions between zonal and eddies and between the baroclinic mode and the barotropic mode, but we hardly observe such separations in the meridional mode domain. The only separation significant in the meridional mode domain may be the symmetric and antisymmetric decomposition. Table 4 lists the symmetric and antisymmetric decomposition of energetics variables of the Rossby mode for the GLA simulation and analysis and the GFDL analysis. The values are the summation of all wavenumbers and vertical modes. The results indicate energy conversions from the symmetric to antisymmetric mode for available potential energy and from the antisymmetric to the symmetric mode for kinetic energy. A large kinetic energy level of the symmetric mode for the GLA simulation is also noted.

The same energetics variables are summarized in Table 5 for the zonal ($s = 0$) and eddy ($s = 1$–15) decomposition together with the barotropic ($m = 0$) and baroclinic ($m = 1$–11) decomposition. For kinetic energy, the GLA simulation indicates a value nearly double the others in the zonal barotropic mode which is related to the large interaction B from the eddy baroclinic mode. Available potential energy is in better agreement between the data sets. The total energy flows from the baroclinic mode to the barotropic mode (sum of D, $m = 1$–11) are 3.31, 2.07 and 4.42 Wm for the GLA simulation and analysis and the GFDL analysis. The total energy flows from the zonal mean to the eddy components (sum of D, $s = 0$) are 2.47, 1.82 and 1.59 Wm. These values compare favorably with the FGGE winter energy budget as reported by Kung and Tanaka (1983) in their standard spectral analysis.

According to the results of the normal mode energetics analysis presented in this study, the characteristic energy flow may be described as

Table 4. *Energy and energy balance of symmetric and antisymmetric decomposition for different data sets*

Data and mode	K	A	E	B	C	D
GLA simulation						
symmetric	20.5	51.1	71.6	0.24	−1.55	1.31
antisymmetric	4.3	5.2	9.5	−0.52	1.19	−0.71
GLA analysis						
symmetric	14.2	47.2	61.4	0.47	−0.90	0.46
antisymmetric	6.1	8.0	14.1	−0.32	1.43	−1.12
GFDL analysis						
symmetric	13.4	48.3	61.8	0.11	−0.53	0.40
antisymmetric	5.0	6.4	11.3	−0.32	0.97	−0.63

Units are 10^5 J m^{-2} for kinetic energy (K), available potential energy (A) and total energy (E), and W m^{-2} for interaction of kinetic energy (B), available potential energy (C) and total diabatic process (D).

Table 5. *Energy and energy balance of zonal mean ($s = 0$) and eddy ($s = 1$–15) components for barotropic ($m = 0$) and baroclinic ($m = 1$–11) decomposition for different data sets*

Data and mode		K	A	E	B	C	D
GLA simulation							
$s = 0$	$m = 0$	11.8	3.2	15.5	0.93	−1.58	0.67
	$m = 1$–11	4.7	48.5	53.2	0.10	−2.06	1.80
$s = 1$–15	$m = 0$	4.0	0.2	4.2	0.72	2.73	−3.37
	$m = 1$–11	4.3	4.3	8.6	−2.02	0.56	1.51
GLA analysis							
$s = 0$	$m = 0$	7.1	2.1	9.2	0.64	−1.29	0.69
	$m = 1$–11	3.7	48.1	51.8	0.07	−1.08	1.13
$s = 1$–15	$m = 0$	4.8	2.8	5.0	0.62	2.71	−3.42
	$m = 1$–11	4.7	4.8	9.5	−1.18	0.19	0.94
GFDL analysis							
$s = 0$	$m = 0$	6.4	1.9	8.3	0.50	1.96	−2.46
	$m = 1$–11	4.2	48.6	52.8	−0.05	−3.96	4.05
$s = 1$–15	$m = 0$	3.6	0.2	3.8	0.34	1.86	−2.20
	$m = 1$–11	4.2	4.0	8.2	−0.99	0.58	0.37

Units are 10^5 J m^{-2} for kinetic energy (K), available potential energy (A) and total energy (E), and W m^{-2} for interaction of kinetic energy (B), available potential energy (C) and total diabatic process (D).

follows. First, the atmospheric energy enters into the zonal baroclinic modes (β_z is approximately 1.0, i.e., available potential energy is dominant). In the case of the GFDL analysis, the mode of $m = 4$, $r = 1$ of $s = 0$ corresponds to this condition. It is noted that there is no such meridional mode for $m = 0$. Part of the energy will be damped by radiational cooling and the remainder will be converted to kinetic energy by baroclinic conversion. This implies that the energy is converted from the initial mode to other modes whose β_z is smaller than 1.0. The computation of β_z shows it decreased from the baroclinic mode to the barotropic mode and also from the zonal to eddy components for the Rossby modes. For this reason, the observed net energy conversion is associated with a decrease of β_z in the s, r and m domains. If only the kinetic energy is concerned, the observed kinetic energy transformation is characterized as from small β_u to large β_u so that u-component of kinetic energy will increase.

The normal mode energetics scheme is a suitable diagnostic tool to depict the energetics of the general circulation in spite of the restriction that the 3-D NMF are obtained for a basic state at rest rather than a realistic zonal basic state. It may

be desirable to use a realistic zonal basic state associated with a proper physical interpretation of each mode. However, the 3-D NMF in a realistic zonal basic state do not satisfy orthonormality, and the associated eigenfrequencies become complex due to the energy supply from the abundant zonal available potential energy of the basic state (baroclinic instability). For this reason, the 3-D NMF for the basic state at rest are more convenient.

6. Concluding remarks

An energetics scheme of three-dimensional normal mode expansion is applied to the GLA analysis data during a 25-day period in the FGGE winter and to parallel simulation data during the same period. References are also made to the diagnosis of the GFDL analysis data.

There are significant differences in the barotropic energy level of the gravity mode between the GLA and GFDL analyses (assimilations). In the GLA analysis, the energy level of this mode is more than three times larger than that by the GFDL analysis. The difference apparently comes from the different assimilation processes. The GFDL data assimilation involves the normal mode initialization, whereas the Euler-backward time integration is applied in the GLA scheme. The barotropic gravity mode in the GLA simulation is damped, probably due to the strong damping effect of the time integration for the high-frequency barotropic mode.

Substantial differences in the energy transformation among the GLA analysis and simulation and the GFDL analysis are noted in the zonal mean field. For the GFDL analysis, a larger amount of energy is generated in the baroclinic mode and dissipated in the barotropic mode. In both the GLA analysis and simulation, energy is generated not only in the baroclinic mode but also in the barotropic mode. This may be attributed to the difference in the vertical profile of diabatic heating which is highly model dependent. Over all the wavenumber domain, however, we see that with the normal mode decomposition, the energy generation in the baroclinic mode is balanced by the the sink in the barotropic mode.

Compared to the GLA analysis, the wavenumber 1 in the GLA simulation appears too weak, particularly for the barotropic component. The simulation kinetic energy is about half that of observation. This is apparently related to the simulation's failure to produce clear, dominant winter blockings as observed in the real atmosphere. The strong zonal wind in the simulation is due to the supply of kinetic energy from wavenumbers 2 and 6 of the baroclinic mode.

The present study may demonstrate utilities of three-dimensional normal mode energetics as a useful diagnostic tool to supplement the standard spectral energetics analysis of the general circulation.

7. Acknowledgements

The authors appreciate the technical assistance of L. K. Gibson, G. Vickers and J. M. McKee. This research was conducted at ECK Research Consulting, Inc. under NASA contract NAS5-28116.

REFERENCES

Baker, W. E. 1983. Objective analysis and assimilation of observational data from FGGE. *Mon. Wea. Rev. 111*, 328–342.

Bengtsson, L., Kanamitsu, M., Kållberg, P. and Uppala, S. 1982. FGGE 4-dimensional data assimilation at ECMWF. *Bull. Amer. Meteorol. Soc. 63*, 29–43.

Cressman, G. P. 1959. An operational objective analysis system. *Mon. Wea. Rev. 87*, 367–374.

Hansen, A. R. and Chen, T. C. 1982. A spectral energetics analysis of atmospheric blocking. *Mon. Wea. Rev. 110*, 1146–1165.

Hoskins, B. J. 1983. Modelling of the transient eddies and their feedback on the mean flow. *Large-scale dynamical processes in the atmosphere*. Hoskins, B. J. and Pearce, R. P., eds. Academic Press, 169–199.

Kalnay, E., Balgovind, R., Chao, W., Edelmann, D., Phaendtner, J., Takacs, L. and Takano, K. 1983. Documentation of the GLAS fourth order general circulation model. NASA Tech. Memo 86064 (NTIS N8424028).

Kalnay-Rivas, E., Bayliss, A. and Storch, J. 1977. The 4th order GISS model of the global atmosphere. *Beitr. Phys. Atmos. 50*, 299–311.

Kalnay-Rivas, E. and Hoitsma, D. 1979. The effect of accuracy, conservation and filtering on numerical weather forecasting. *Proc. Fourth Conf. Numerical Weather Prediction*, Silver Spring, Amer. Meteor. Soc., 302–312.

Kasahara, A. 1976. Normal modes of ultralong waves in the atmosphere. *Mon. Wea. Rev. 104*, 669–690.

Kasahara, A. 1984. The linear response of a stratified global atmosphere to tropical thermal forcing. *J. Atmos. Sci. 41*, 2217–2237.

Kasahara, A. and Puri, K. 1981. Spectral representation of three-dimensional global data by expansion in normal mode functions. *Mon. Wa. Rev. 109*, 37–51.

Kung, E. C. 1966. Kinetic energy generation and dissipation in the large-scale atmospheric circulation. *Mon. Wea. Rev. 94*, 67–82.

Kung, E. C. and Tanaka, H. 1983. Energetics analysis of the global circulation during the special observation periods of FGGE. *J. Atmos. Sci. 40*, 2575–2592.

Labitzke, K. 1982. On the interannual variability of the middle stratosphere during the northern winters. *J. Meteorol. Soc. Japan 60*, 124–139.

Leith, C. E. 1971. Atmospheric predictability and two-dimensional turbulence. *J. Atmos. Sci. 28*, 145–161.

Matsuno, T. 1966a. Quasi-geostrophic motions in the equatorial area. *J. Meteorol. Soc. Japan 44*, 25–43.

Matsuno, T. 1966b. Numerical integrations of the primitive equations by a simulated backward-difference method. *J. Meteorol. Soc. Japan 44*, 76–84.

Miyakoda, K., Sheldon, J. and Sirutis, J. 1982. Four-dimensional analysis experiment during the GATE period. Part II. *J. Atmos. Sci. 39*, 486–506.

Ploshay, J. J., White, R. K. and Miyakoda, K. 1983. FGGE Level IIIb daily global analyses, Part I (Dec. 1978–Feb. 1979). Geophysical Fluid Dynamics Laboratory/NOAA, Princeton, New Jersey, 278 pp.

Saltzman, B. 1957. Equations governing the energetics of the larger scales of atmospheric turbulence in the domain of wavenumber. *J. Meteorol. 14*, 513–523.

Shapiro, R. 1970. Smoothing, filtering, and boundary effects. *Rev. Geophys. Space Phys. 8*, 359–387.

Smagorinsky, J. 1963. General circulation experiments with the primitive equations. I: The basic experiment. *Mon. Wea. Rev. 91*, 99–164.

Tanaka, H. 1985. Global energetics analysis by expansion into three-dimensional normal mode functions during the FGGE winter. *J. Meteorol. Soc. Japan. 63*, 180–200.

Wiin-Nielsen, A. 1962. On transformation of kinetic energy between the vertical shear flow and the vertical mean flow in the atmosphere. *Mon. Wea. Rev. 90*, 311–323.

Wiin-Nielsen, A. 1967. On the annual variation and spectral distribution of atmospheric energy. *Tellus 19*, 540–559.